Supporting Information for

Engineering Energy Bands in 0D-2D Hybrid Photodetectors: Cu-Doped InP Quantum Dots on Type-III $SnSe_2/MoTe_2$ Heterojunction

Jiabin Li[a]†, Dongxue Wang[a]†, Xiya Chen[a], Yao Zhou[a], Huanteng Luo[a], Tu Zhao[a], Sheng Hu[a], Zhaoqiang Zheng[b], Wei Gao[a*], Xiao Liu[a*]

[a] Guangdong Provincial Key Laboratory of Chip and Integration Technology, School of Electronic Science and Engineering (School of Microelectronics), Faculty of Engineering, South China Normal University, Foshan 528200, P. R. China.

[b] College of Materials and Energy, Guangdong University of Technology, Guangzhou 510006, P.R. China.

† Jiabin Li and Dongxue Wang contributed equally to this work.

***Corresponding authors:**

Wei Gao, E-mail: gaowei317040@m.scnu.edu.cn

Xiao Liu, E-mail: liuxiao@m.scnu.edu.cn

Note S1: Calculation of the band structure of InP/ZnSeS:Cu/ZnS QDs

$$(\alpha h\nu)^{1/n} = A(h\nu - E_g)$$

$$E_{v,NHE} = \varphi + E_{VB-XPS} - 4.44\ eV$$

$$E_v = -4.5 - E_{v,NHE}$$

$$E_g = E_c - E_v$$

Where α is the absorption coefficient, n = 2, hν is the photon energy, h is Planck's constant (h ≈ 4.13567×10^{-15} eV·s), ν is the frequency of the incident photon. A is the proportionality constant. E_g is the bandgap. $E_{v,\ NHE}$ is normal hydrogen electrode potential, the φ is the electron work function of the XPS analyzer, the value is 4.50 eV, and $E_{VB-\ XPS}$ is valence band maximum value was tested by VB-XPS.[1, 2]

Note S2: Calculation of surface potential difference (SPD)

The SPD between $SnSe_2$ and $MoTe_2$ is extracted by KPFM. Firstly, the SPD between the 2D materials and the KPFM tip can be defined as:

$$eSPD_{SnSe_2} = W_{Tip} - W_{SnSe_2}$$

$$eSPD_{MoTe_2} = W_{Tip} - W_{MoTe_2}$$

Where e is elementary charge, W_{Tip}, W_{SnSe_2} and W_{MoTe_2} are the work function of the KPFM tip, $SnSe_2$ and $MoTe_2$, respectively. Thus, the SPD and the difference of Fermi level between $SnSe_2$ and $MoTe_2$ (ΔE_f) can be calculated by:

$$\Delta E_f = SPD_{MoTe_2} - SPD_{SnSe_2}$$

In this work, the SPD between $SnSe_2$ and $MoTe_2$ is 25 mV.[3]

Note S3: Calculation the photovoltaic effect in the photodetectors

To better evaluate the photovoltaic effect of $SnSe_2/MoTe_2$ and $InP/SnSe_2/MoTe_2$ devices, electrical power (P_{el}), photoelectric conversion efficiency (PCE) and fill factor (FF) are key quality factors.[3]

$$P_{el} = V_{ds} I_{ds}$$

$$FF = \frac{P_{elmax}}{V_{oc} I_{sc}}$$

$$PCE = \frac{P_{elmax}}{P_{in}}$$

Note S4: Calculation of the key figures-of-merit for photodetectors

To better evaluate the optoelectronic performance of $SnSe_2/MoTe_2$ and $InP/SnSe_2/MoTe_2$ devices, important parameters including responsivity (R), detectivity (D^*), external quantum efficiency (EQE), light on/off ratio (I_{light}/I_{dark}), and response time (τ_{rise} and τ_{decay}) are calculated. These figures-of-merit can be calculated by the following equations:

$$R = \frac{I_{ph}}{PS} = \frac{I_{light} - I_{dark}}{PS}$$

$$D^* = \frac{R\sqrt{S}}{\sqrt{2qI_{dark}}} = \frac{R\sqrt{S}}{S_n} = \frac{\sqrt{BS}}{S_n}$$

$$EQE = \frac{hcI_{ph}}{\lambda qPS} = \frac{hcR}{\lambda q}$$

where q is the electronic charge, S is the effective sensing area, and P is the incident light density, B is noise bandwidth, h is the Planck constant (6.626×10^{-34} J s^{-1}), c is the light velocity, λ is the wavelength of the incident light, I_{ph} is the photocurrent ($I_{ph} = I_{light} - I_{dark}$), I_{light} and I_{dark} are the device current under light and dark, respectively. In the time domain, rise time (τ_{rise}) and decay time (τ_{decay}) are defined as the time interval required from 10 %/90 % to 90 %/10 % of the net photocurrent.[4, 5]

Note S5: Analyze direct tunneling (DT) and band-to-band tunneling (BTBT) of the photo-induced carriers

In order to further verify tunneling mechanism of devices, the forward current transport across the heterostructure can be modeled by the Simmons approximation.[6, 7]

$$I_{DT} \propto V exp\left(-\frac{4\pi\sqrt{2m^*\varphi}}{h}\right)$$

or

$$\ln\left(\frac{1}{V^2}\right) \propto ln\left(\frac{1}{V}\right) - \frac{4\pi d\sqrt{2m^*\varphi}}{h}$$

$$I = C_1V^2 exp(\frac{C_2}{V})$$

where V is the bias voltage, m^* is effective mass of the carrier, q is the element charge, h is the Planck constant, d is the width of the tunneling barrier, φ is the barrier height, and C_1 and C_2 are constants. Under negative bias voltage, The E_v of $MoTe_2$ exceeds the E_c of $SnSe_2$. This causes electrons to move from the valence band (VB) of $MoTe_2$ to the BTBT of CB of $SnSe_2$, resulting in a reverse current of the Zener diode. Under positive bias voltage, the thermionic emission or thermal-assisted tunneling of majority carriers from the conduction band (CB) of $SnSe_2$ to the CB of $MoTe_2$ dominates the transport across the $SnSe_2/MoTe_2$ heterojunction, resulting in the re-increase of current. The band alignments of $SnSe_2/MoTe_2$ heterojunction at negative and positive bias voltage see in Figure S16. In the dark, the heterojunction serves as a backward diode in which the electrons cannot tunnel through the interfacial barrier at a forward bias. After illumination, excess carriers are generated on both sides of $MoTe_2$ and $SnSe_2$, and accumulate at the interface due to the internal electric field. This increases the Fermi level difference between $MoTe_2$ and $SnSe_2$, which is favorable for photogenic electrons to tunnel from CB of $SnSe_2$ to CB of $MoTe_2$ through the DT process.

Note S6: Preparation of absorbed samples

Before measurement, $SnSe_2$ and $MoTe_2$ were exfoliated onto a PDMS film, while $MoTe_2$ was transferred onto a 1 ×1 cm transparent sapphire substrate using a double toss via dry transfer method. The $SnSe_2/MoTe_2$ heterojunction (Sample I) was fabricated using a simple three-axis manipulator platform equipped with a micromanipulator through the dry transfer method. The corresponding overlapped area of Sample I is 124 μm^2. For the InP QDs/$SnSe_2$/$MoTe_2$ heterostructure, it was achieved by the directly spin-coating process on the $SnSe_2$/$MoTe_2$ heterostructure on the sapphire substrate. During the measurement, the diameter of the measured spot was as small as 5 μm, which was used to illuminate the overlapped area shown in Fig. S7a.

Figures:

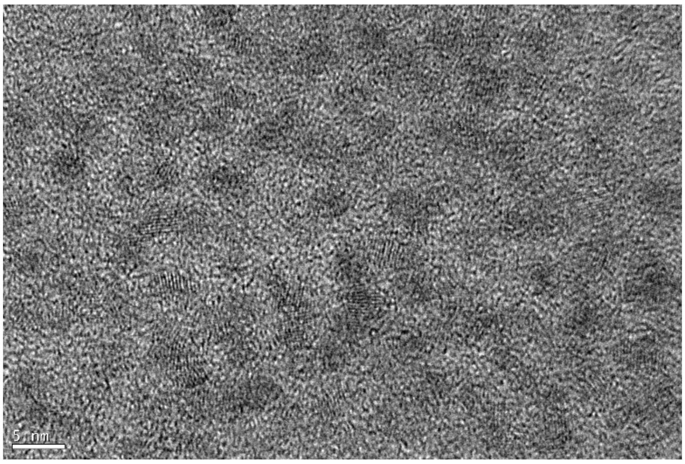

Figure S1. HRTEM image of InP/ZnSeS:Cu/ZnS QDs.

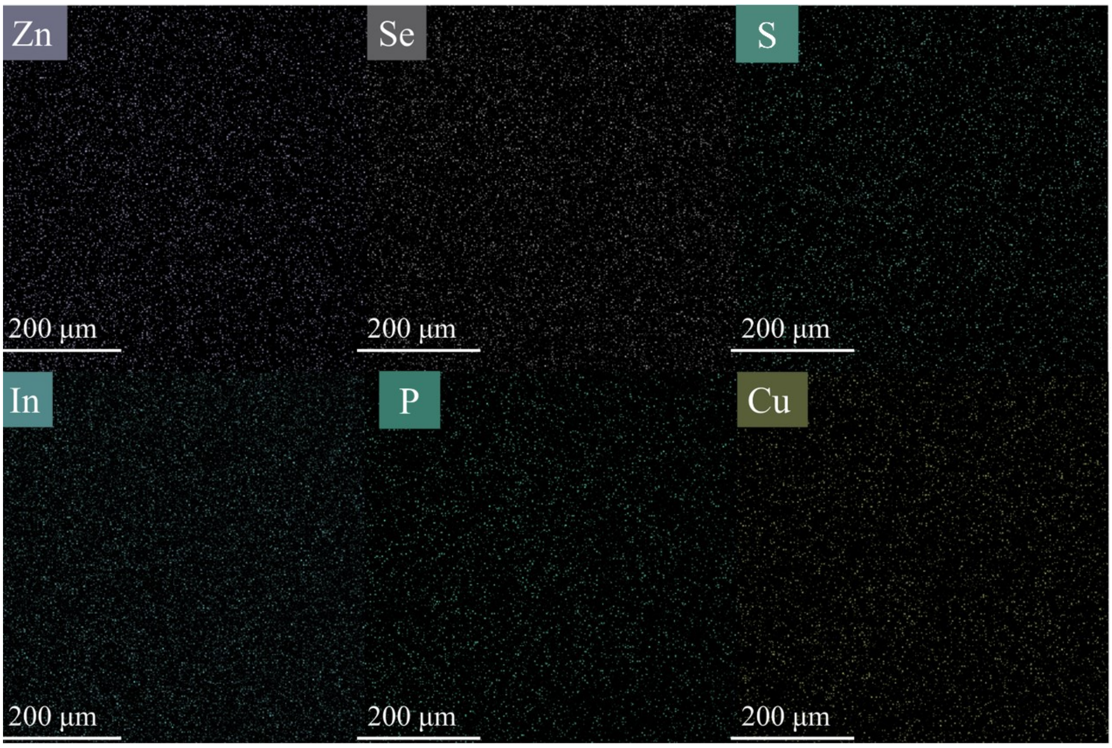

Figure S2. EDS element mapping of InP/ZnSeS:Cu/ZnS QDs.

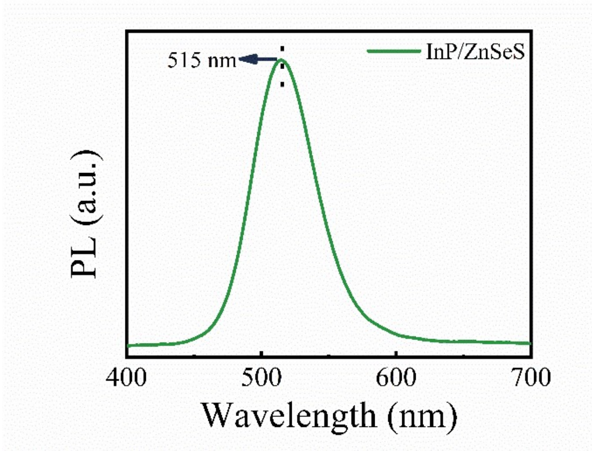

Figure S3. PL of InP/ZnSeS before Cu doped.

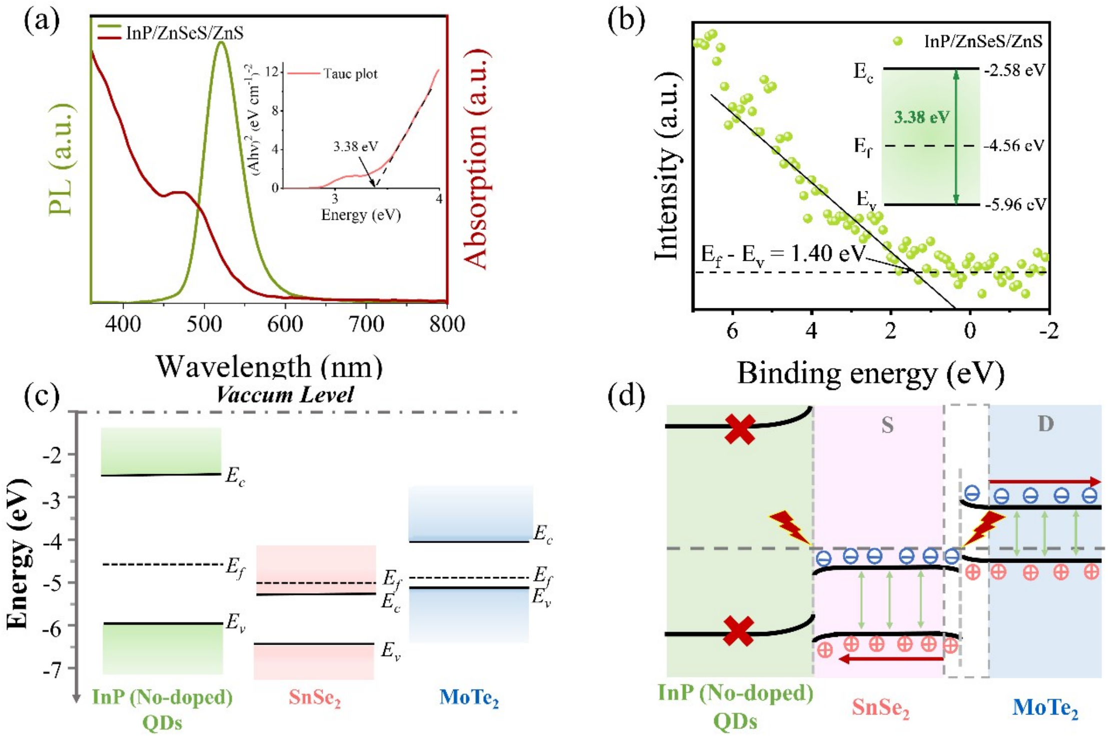

Figure S4. (a) Absorption (red lines) and PL (green lines) spectra of InP/ZnSeS/ZnS QDs. The inset shows the converted Kubelka-Munk functions in relation to their photon energy. (b) The band structure of InP/ZnSeS/ZnS QDs alignments estimated based on the UV–Vis absorption spectra and VB-XPS data. The inset shows the energy band diagram. (c) Energy band diagram of the InP(No-doped)/$SnSe_2$/$MoTe_2$ heterostructure prior to contact. (d) Band diagram and current transport mechanism of the InP(No-doped)/$SnSe_2$/$MoTe_2$ heterojunction under 532 nm laser illumination.

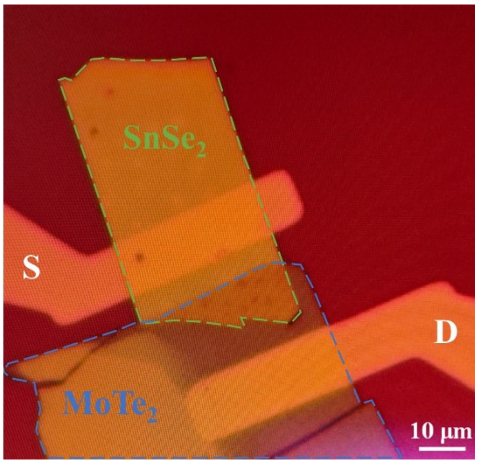

Figure S5. Optical microscopic image of $SnSe_2/MoTe_2$ for Device I before spin-coating.

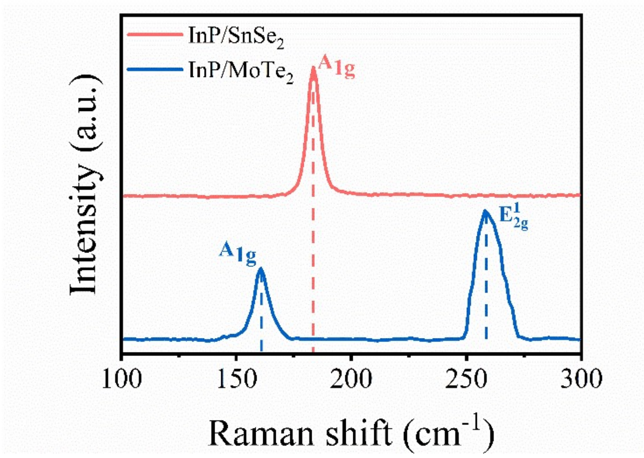

Figure S6. Raman spectra of $InP/MoTe_2$ and $InP/SnSe_2$.

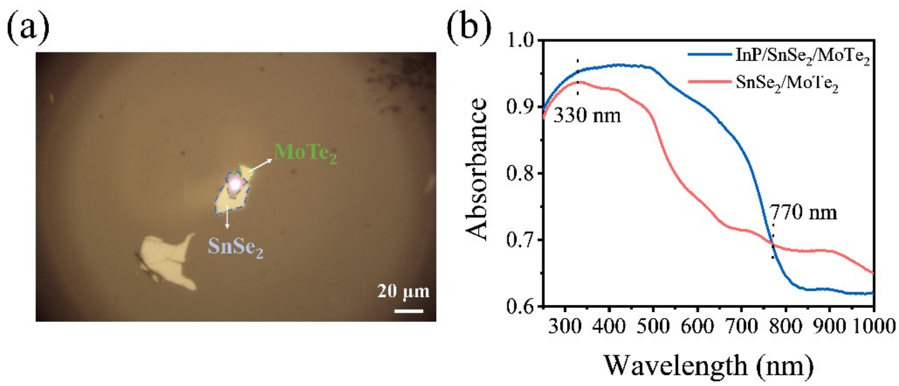

Figure S7. (a) Sample picture on sapphire. (b) Absorption spectra of $SnSe_2/MoTe_2$ and $InP/SnSe_2/MoTe_2$.

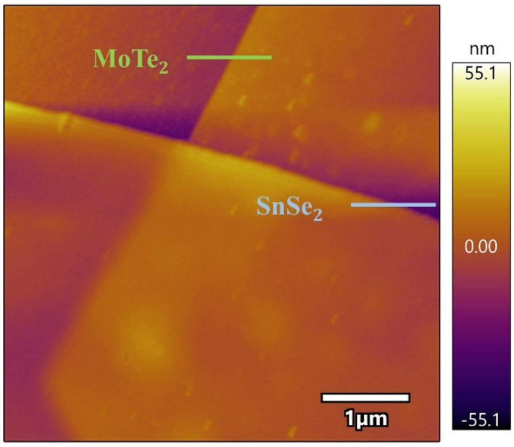

Figure S8. AFM image of the $SnSe_2/MoTe_2$ heterojunction Device I.

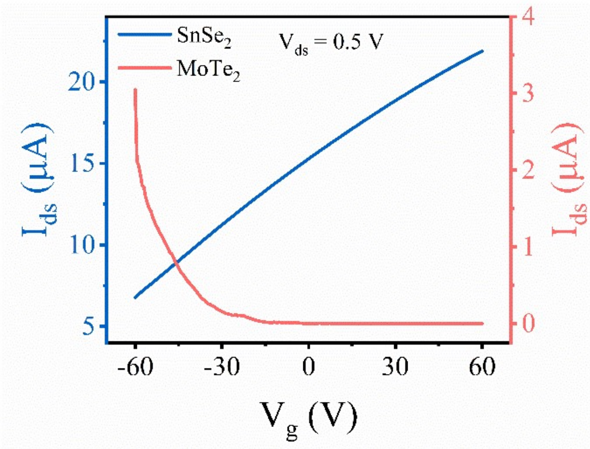

Figure S9. Transfer curves of multilayered $MoTe_2$ and $SnSe_2$ in Device I.

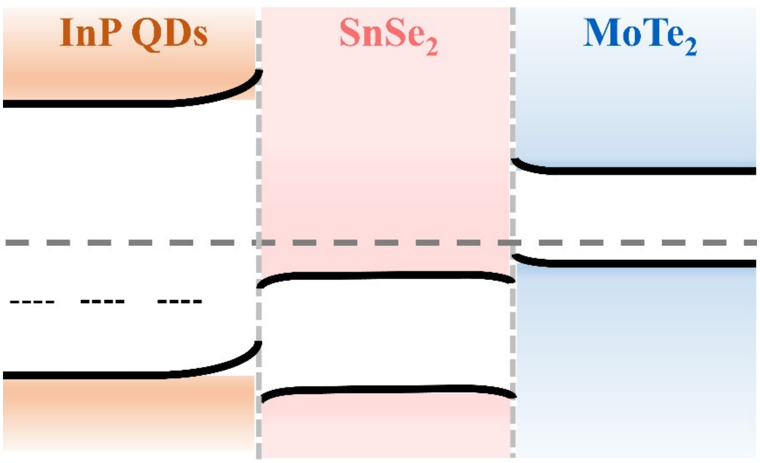

Figure S10. Energy band diagram of the $InP/SnSe_2/MoTe_2$ heterostructure after contact at zero bias.

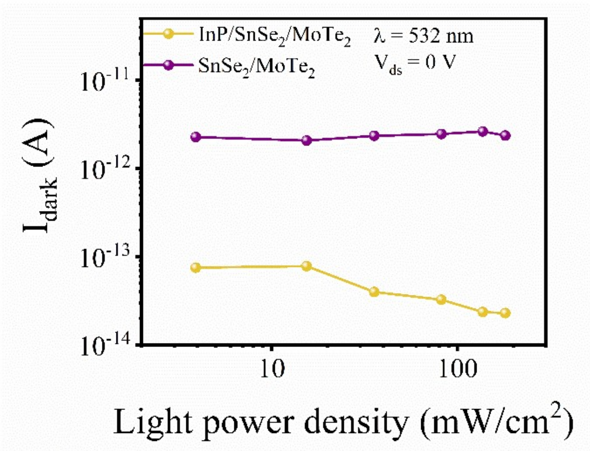

Figure S11. I_{dark} of InP/$SnSe_2$/$MoTe_2$ and $SnSe_2$/$MoTe_2$ in Device I at different light power densities.

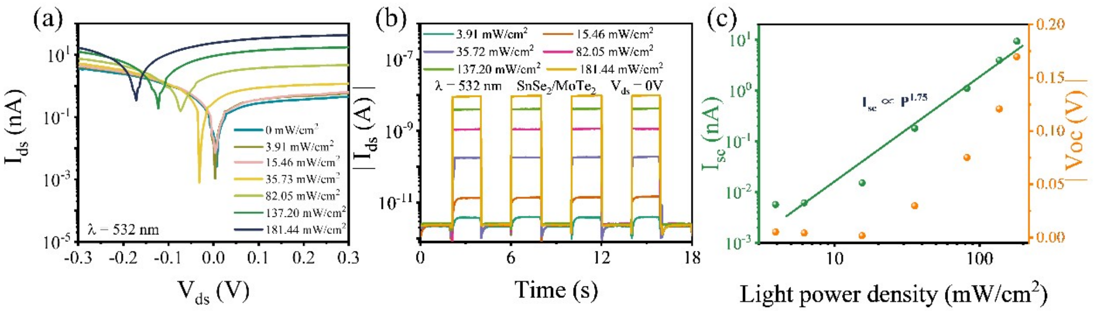

Figure S12. The photoelectric characteristics of $SnSe_2$/$MoTe_2$ Device I. (a) I_{ds}-V_{ds} characteristics with respect to incident light power density. (b) The time-resolved photoresponse at different light power densities. (c) Variation of I_{sc} and V_{oc} with light power density.

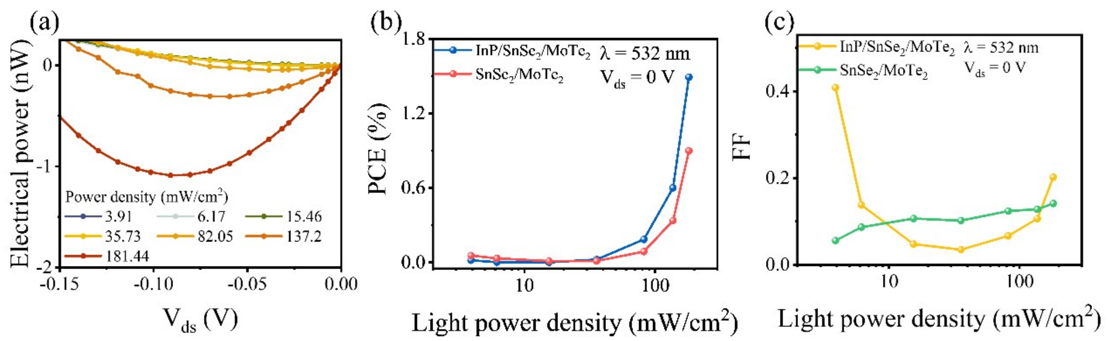

Figure S13. (a) $SnSe_2$/$MoTe_2$ the electrical power as a function of V_{ds} under different light power densities. (b) (c) PCE and FF of Device I as a function of light power density under 532 nm.

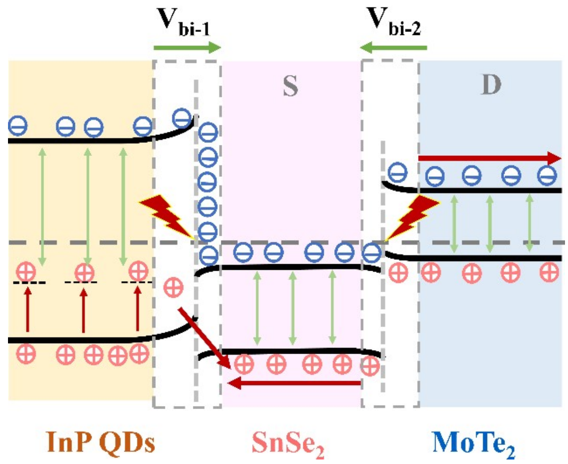

Figure S14. Band diagram and current transport mechanism of the InP/$SnSe_2$/$MoTe_2$ heterojunction under high light power density at 532 nm.

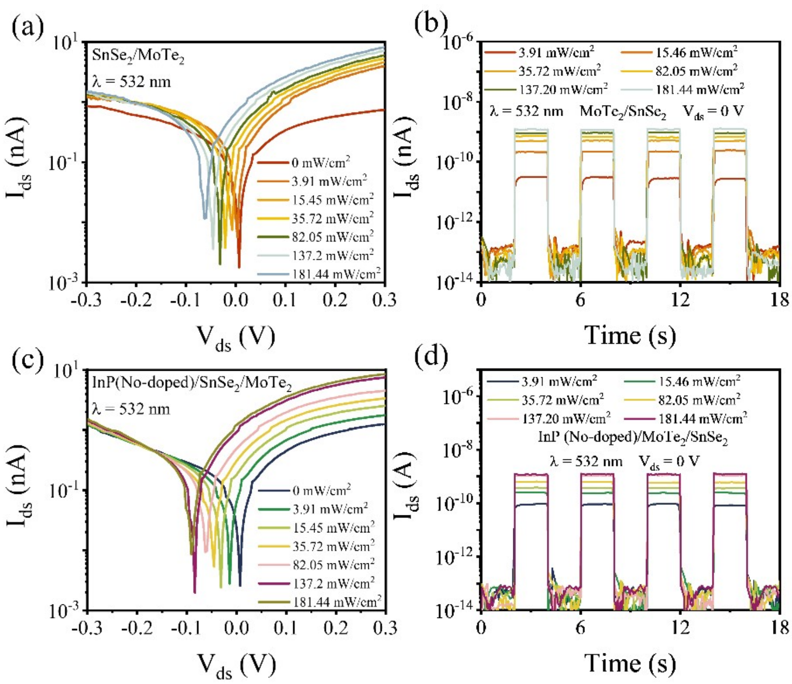

Figure S15. (a) (c) I_{ds}-V_{ds} characteristics of $SnSe_2$/$MoTe_2$ and InP(No-doped)/$SnSe_2$/$MoTe_2$ heterostructure with respect to incident light power density. (b) (d) The time-resolved photoresponse of $SnSe_2$/$MoTe_2$ and InP(No-doped)/$SnSe_2$/$MoTe_2$ heterostructure at different light power densities.

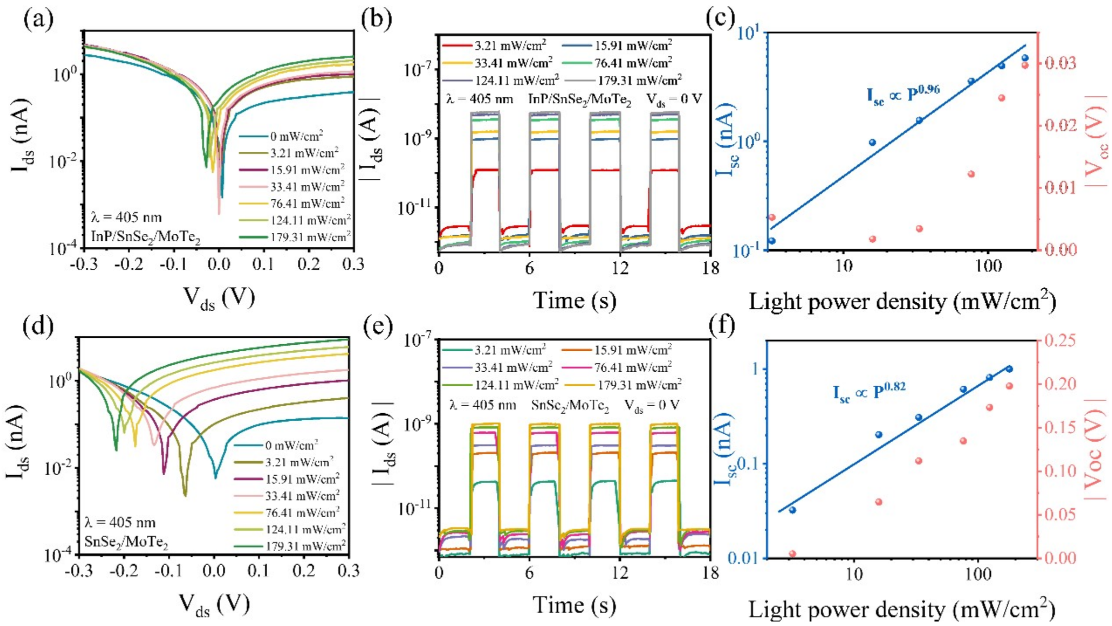

Figure S16. Photovoltaic properties of Device I under 405 nm laser. (a) (d) $I_{ds}-V_{ds}$ curves of the Device I under different light power densities. (b) (e) The time-resolved photoresponse at different light power densities. (c) (f) Variation of I_{sc} and V_{oc} with light power density.

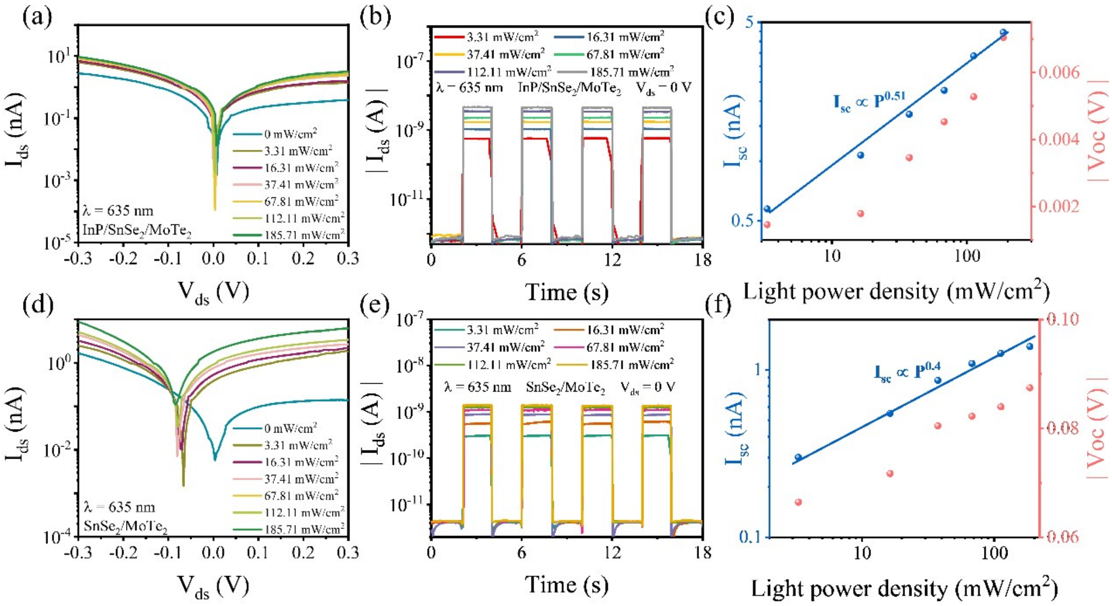

Figure S17. Photovoltaic properties of Device I under 635 nm laser. (a) (d) $I_{ds}-V_{ds}$ curves of the Device I under different light power densities. (b) (e) The time-resolved photoresponse at different light power densities. (c) (f) Variation of I_{sc} and V_{oc} with light power density.

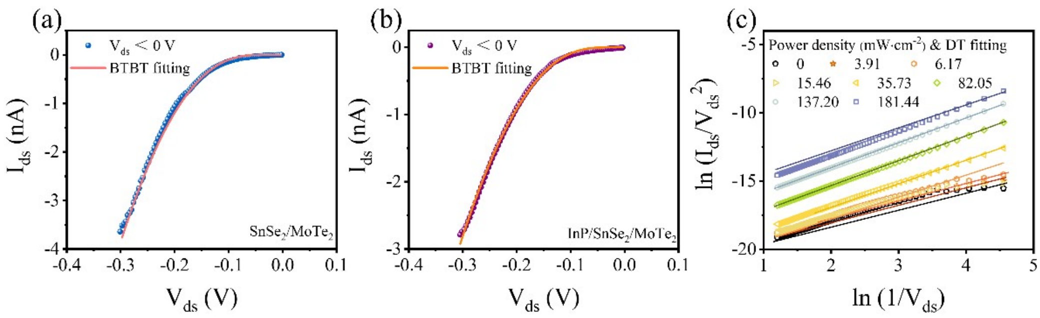

Figure S18. (a) (b) Band-to-band tunneling (BTBT) plots fitting of backward current for Device I. (c) DT plots of ln (I_{ds}/V_{ds}^2) and ln ($1/V_{ds}$) obtained from Figure S11(b). The solid line represents the DT fitting curve of the experimental data.

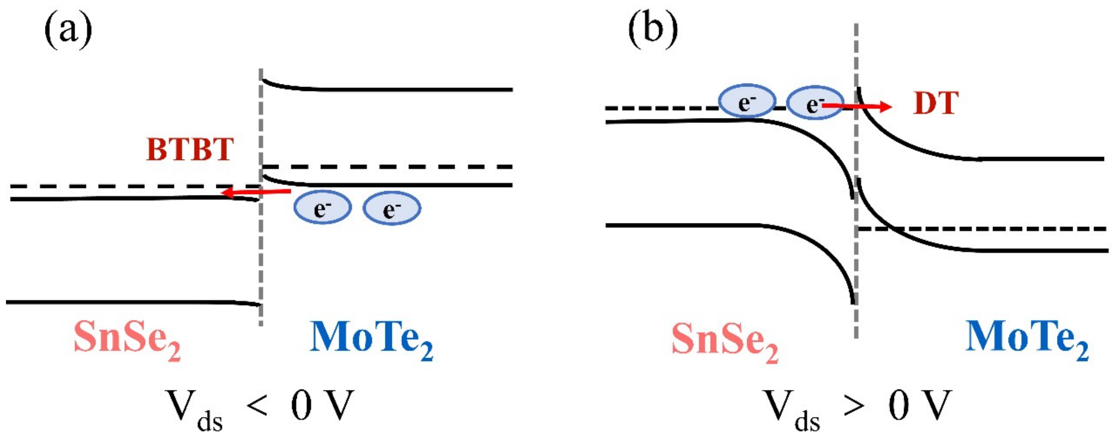

Figure S19. Schematic band alignments of $SnSe_2/MoTe_2$ heterojunction at $V_{ds}<0$ V and $V_{ds}>0$ V.

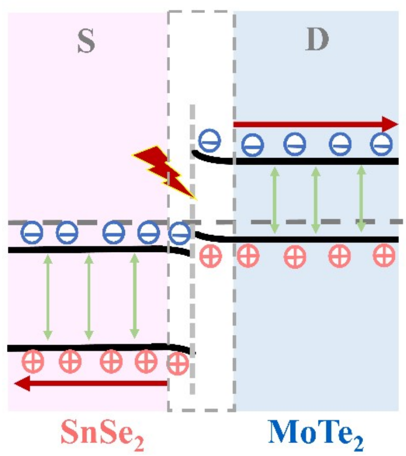

Figure S20. Band diagram and charge transport mechanism of the $SnSe_2/MoTe_2$ heterojunction under illumination.

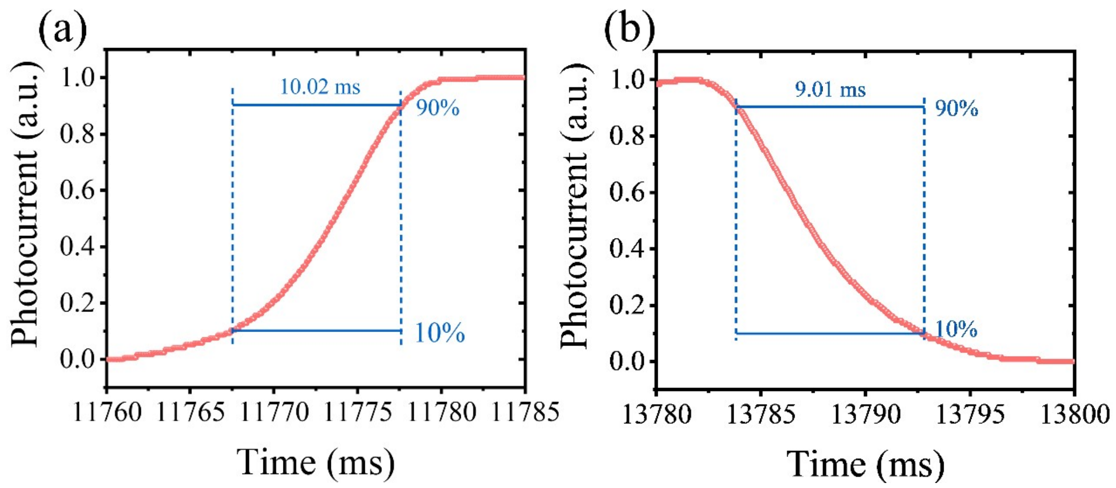

Figure S21. Photovoltaic rising/decaying time. (a) (b) Time-solved photocurrent of the $SnSe_2/MoTe_2$ heterojunction for Device I before spin-coating.

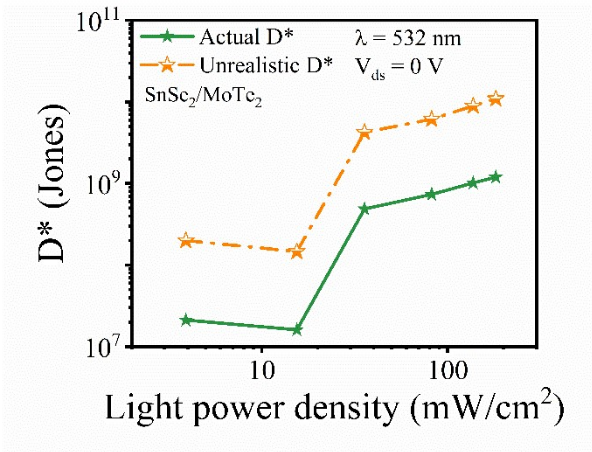

Figure S22. The unrealistic D^* and the actual D^* of $SnSe_2/MoTe_2$ as a function of the incident light power density.

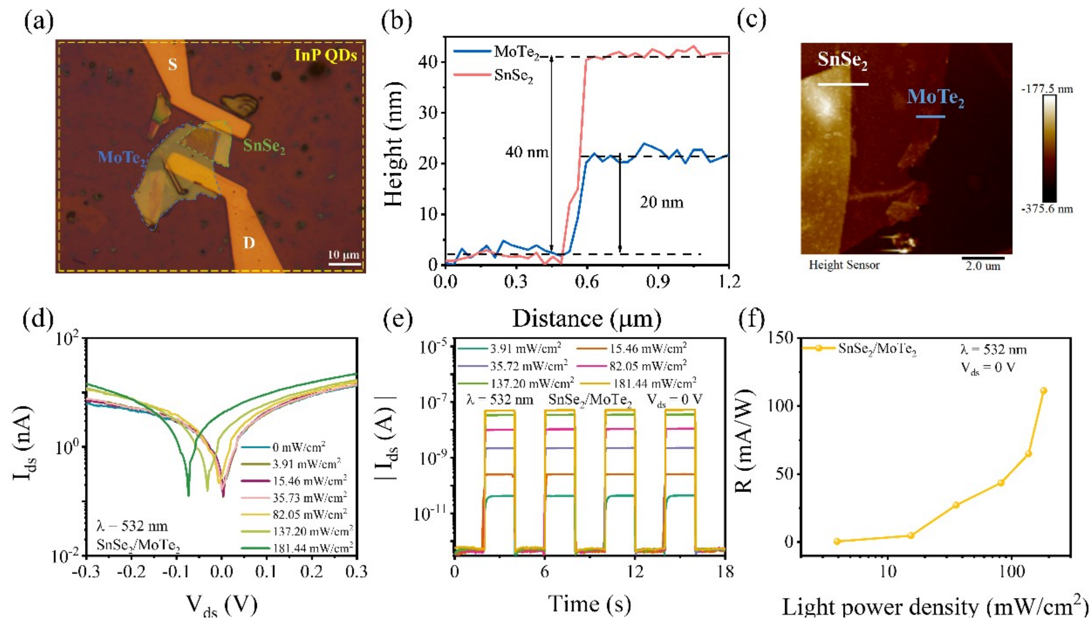

Figure S23. The photoelectric characteristics of Device II under 532 nm laser. (a) Optical microscopic images of InP/$SnSe_2$/$MoTe_2$. (b) Height profiles of $MoTe_2$ and $SnSe_2$. (c) AFM image of the $SnSe_2$/$MoTe_2$ heterojunction. (d) I_{ds}-V_{ds} curves of the $SnSe_2$/$MoTe_2$ under different light power densities. (c) The time-resolved photoresponse of $SnSe_2$/$MoTe_2$ at different light power densities.

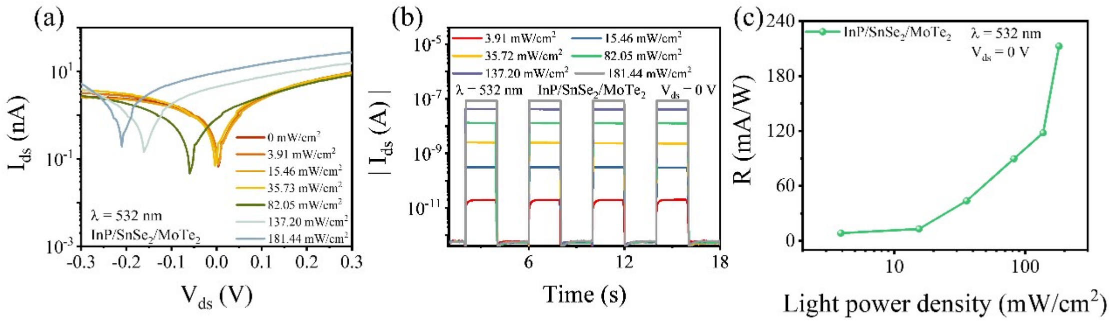

Figure S24. The photoelectric characteristics of Device II under 532 nm laser. (a) I_{ds}-V_{ds} curves of the InP/$SnSe_2$/$MoTe_2$ under different light power densities. (b) The time-resolved photoresponse of InP/$SnSe_2$/$MoTe_2$ at different light power densities. (c) R of Device I as a function of light power density.

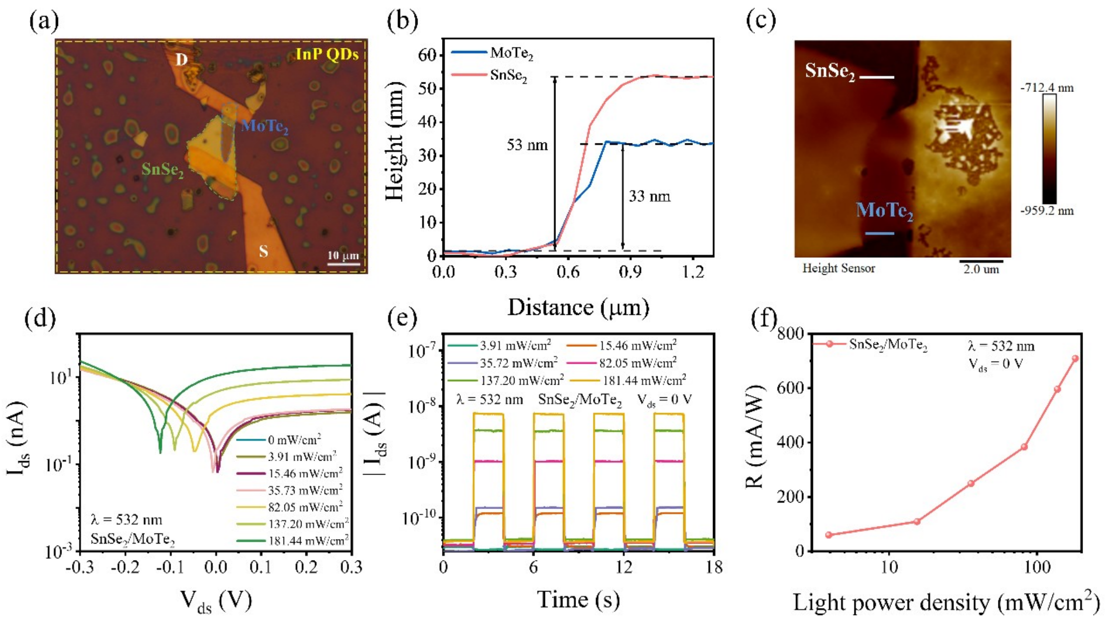

Figure S25. The photoelectric characteristics of Device III under 532 nm laser. (a) Optical microscope images of Device III. (b) Height profiles of $MoTe_2$ and $SnSe_2$. (c) AFM image of the $SnSe_2/MoTe_2$ heterojunction. (d) I_{ds}-V_{ds} curves of the $SnSe_2/MoTe_2$ under different light power densities. (c) The time-resolved photoresponse of $SnSe_2/MoTe_2$ at different light power densities.

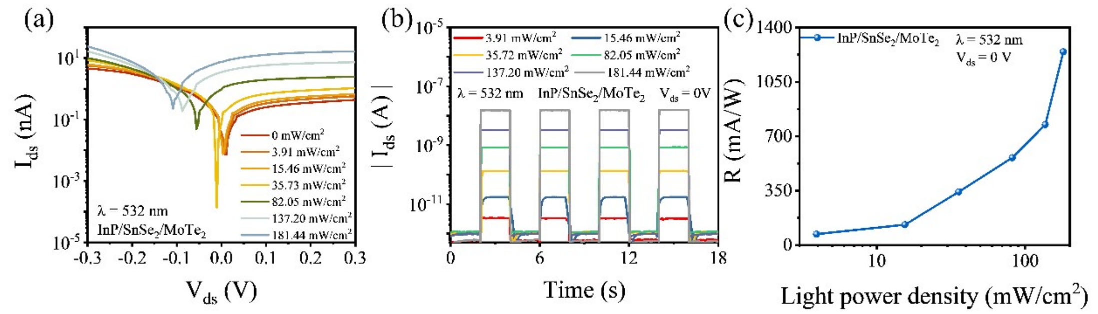

Figure S26. The photoelectric characteristics of Device III under 532 nm laser. (a) I_{ds}-V_{ds} curves of the $InP/SnSe_2/MoTe_2$ under different light power densities. (b) The time-resolved photoresponse of $InP/SnSe_2/MoTe_2$ at different light power densities. (c) R of Device III as a function of light power density.

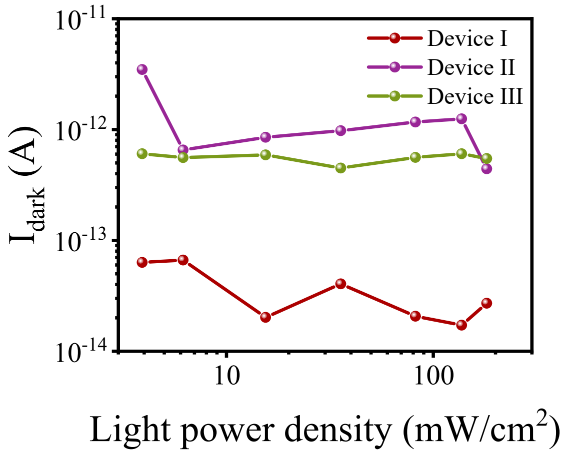

Figure S27. I_{dark} of InP/$SnSe_2$/$MoTe_2$ in Device I, Device II and Device III at different light power densities.

References

1. X. Chen, Y. Guo, J. Li, H. Yang, Z. Chen, D. Luo and X. Liu, *Chem. Eng. J.*, 2024, **496**.
2. R. G. Xie and X. G. Peng, *J. Am. Chem. Soc.*, 2009, **131**, 10645-10651.
3. J. Ma, S. Chen, L. Zhao, J. Chen, Z. Lan, M. Yang, Y. Sun, Z. Zheng, W. Gao and J. Li, *Adv. Opt. Mater.*, 2024, **12**.
4. H. Shang, Y. Hu, F. Gao, M. Dai, S. Zhang, S. Wang, D. Ouyang, X. Li, X. Song, B. Gao, T. Zhai and P. Hu, *ACS Nano*, 2022, **16**, 21293-21302.
5. Z. Li, T. Zheng, M. Yang, Y. Sun, D. Luo, W. Gao, Z. Zheng and J. Li, *Adv. Opt. Mater.*, 2024, **12**.
6. S. Kim, H. Du, T. Kim, S. Shin, H.-k. Song, H. Kim, D. Kang, C.-W. Lee and S. Seo, *Npj 2d Materials and Applications*, 2020, **4**.
7. S. Chen, J. Ma, N. Bu, T. Zheng, J. Chen, J. Huang, X. Luo, Z. Zheng, N. Huo, J. Li and W. Gao, *ACS Appl. Mater. Interfaces*, 2024, **16**, 33740-33751.